Biosensors and Bioelectronics 177 (2021) 112672

Contents lists available at ScienceDirect

Biosensors and Bioelectronics

journal homepage: http://www.elsevier.com/locate/bios

Enhancing the performance of paper-based electrochemical impedance spectroscopy nanobiosensors: An experimental approach

Xiao Li [a,b], Zhen Qin [c], Hao Fu [a], Ted Li [a], Ran Peng [c], Zhijie Li [d], James M. Rini [d], Xinyu Liu [a,c,e,*]

[a] Department of Mechanical Engineering, McGill University, Montreal, QC, Canada
[b] Department of Chemistry, Stanford University, Stanford, CA, USA
[c] Department of Mechanical and Industrial Engineering, University of Toronto, Toronto, ON, Canada
[d] Department of Biochemistry, University of Toronto, Toronto, ON, Canada
[e] Institute of Biomedical Engineering, University of Toronto, Toronto, ON, Canada

ARTICLE INFO

Keywords:
Point-of-care diagnosis
Microfluidic paper-based analytical devices
Electrochemical impedance biosensing
Nanowires
HIV
COVID-19

ABSTRACT

Accurate, rapid, and low-cost molecular diagnostics is essential in managing outbreaks of infectious diseases, such as the pandemic of coronavirus disease 2019 (COVID-19). Accordingly, microfluidic paper-based analytical devices (μPADs) have emerged as promising diagnostic tools. Among the extensive efforts to improve the performance and usability of diagnostic tools, biosensing mechanisms based on electrochemical impedance spectroscopy (EIS) have shown great promise because of their label-free operation and high sensitivity. However, the method to improve EIS biosensing on μPADs is less explored. Here, we present an experimental approach to enhancing the performance of paper-based EIS biosensors featuring zinc oxide nanowires (ZnO NWs) directly grown on working electrodes (WEs). Through a comparison of different EIS settings and an examination of ZnO-NW effects on EIS measurements, we show that ZnO-NW-enhanced WEs function reliably with Faradaic processes utilizing iron-based electron mediators. We calibrate paper-based EIS biosensors with different morphologies of ZnO NWs and achieve a low limit of detection (0.4 pg ml^{-1}) in detecting p24 antigen as a marker for human immunodeficiency virus (HIV). Through microscopic imaging and electrochemical characterization, we reveal that the morphological and the electrochemical surface areas of ZnO-NW-enhanced WEs indicate the sensitivities and sensing ranges of the EIS nanobiosensors. Finally, we report that the EIS nanobiosensors are capable of differentiating the concentrations (blank, 10 ng ml^{-1}, 100 ng ml^{-1}, and 1 μg ml^{-1}) of IgG antibody (CR3022) to SARS-CoV-2 in human serum samples, demonstrating the efficacy of these devices for COVID-19 diagnosis. This work provides a methodology for the rational design of high-performance EIS μPADs and has the potential to facilitate diagnosis in pandemics.

1. Introduction

In recent decades, humanity has been recurrently suffering from severe outbreaks of infectious diseases, including human immunodeficiency virus (HIV), severe acute respiratory syndrome (SARS), swine flu H1N1, middle east respiratory syndrome (MERS), and currently the coronavirus disease 2019 (COVID-19) (Wang et al., 2020; Zhu et al., 2019). These outbreaks have caused tremendous casualties and economic burdens (Bhutta et al., 2014). Particularly, the pandemic of COVID-19 has led to a tremendous scale of lockdown and economic stasis. Identifying infected persons as early as possible is critical for effective quarantines that can substantially slow down the disease spreading. However, due to the vast number of infected people and the shortage of healthcare professionals and medical facilities, laboratory-based diagnostic tests are far from sufficient (McBain et al., 2016). Therefore, accurate, affordable, and rapid diagnostic tools that can be distributed and implemented outside clinical laboratories have great potential to help manage such crises (Wang et al., 2020; Martinez et al., 2010; Perkins, 2011).

Among the diagnostic tools devised over the past decades, microfluidic paper-based analytical devices (μPADs) for point-of-care (POC) diagnosis have stood out as a particularly promising platform technology, leveraging the intrinsic properties of paper such as amenability to chemical and physical modifications, disposability, capillarity-driven liquid manipulation, and potential for mass production (Gong and Sinton, 2017; Chen et al., 2019; Rolland and Mourey, 2013; Ying et al.,

* Corresponding author. Department of Mechanical Engineering, McGill University, Montreal, QC, Canada.
E-mail address: xyliu@mie.utoronto.ca (X. Liu).

https://doi.org/10.1016/j.bios.2020.112672
Received 28 April 2020; Received in revised form 24 August 2020; Accepted 30 September 2020
Available online 12 October 2020

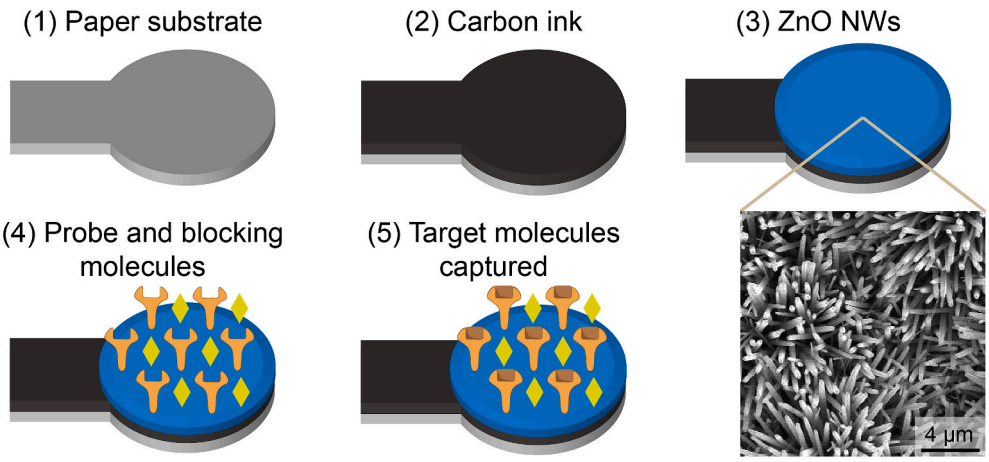

Fig. 1. Fabrication and surface functionalization of paper-based WEs for EIS biosensing. As a key component in EIS biosensing, WEs were prepared and used in five steps: (1) cutting paper pieces into the shape of WEs, (2) printing a layer of carbon ink to the paper pieces, (3) growing ZnO NWs on the carbon ink, (4) immobilizing probe and blocking molecules to the surface of WEs, and (5) eventually using the WEs to capture target molecules for EIS biosensing.

2020). These devices are normally used for the detection of biomarkers in body fluids, featuring low-cost fabrication and convenient assay operations (Gong and Sinton, 2017; Yang et al., 2017). Therefore, they could address the world health organization's "ASSURED" (affordable, sensitive, specific, user-friendly, rapid and robust, equipment-free and deliverable to end-users) criteria for diagnostic tools and help meet the soaring demands for POC diagnosis in an epidemic or pandemic.

To fulfill their potential, μPADs ought to have detection performance at least comparable to the gold standard tests (Sher et al., 2017; Yamada et al., 2017). A large body of research on μPADs utilizes working principles similar to enzyme-linked immunosorbent assays (ELISAs) (Cheng et al., 2010; Martinez, 2011; Fu et al., 2019) because the detection of protein markers is essential to dealing with outbreaks like HIV and COVID-19. However, these assays often require multiple labeling and amplifying steps, making the assay operations less convenient and prone to errors. Given the limitations of ELISAs, electrochemical impedance sensing (EIS) has gained increasing research interest. EIS-based biosensing mechanisms inherently require no labels, which simplifies the assay operations. With appropriate settings and interpretation of EIS measurements, one can achieve high sensitivity. For example, paper-based EIS biosensors have been reported for label-free detection of bacteria (Rengaraj et al., 2018) and protein biomarkers (Ruecha et al., 2019). In another study, single-frequency EIS measurements on paper-based biosensors have been proposed to achieve even more convenient assay operations (Rengaraj et al., 2018; Zhao and Liu, 2016). These studies typically utilized carbon ink printed on paper substrates as working electrodes (WEs), which play an essential role in EIS biosensing. To improve the EIS WEs, we have recently reported that zinc oxide nanowires (ZnO NWs) could be directly synthesized on the carbon-ink electrodes for EIS biosensing on μPADs (Li and Liu, 2016). We showed that the combination of EIS and ZnO NWs could achieve highly sensitive detection of protein biomarkers. Despite the great potential of ZnO-NW-enhanced EIS biosensing on μPADs, the reliable settings of EIS measurements and the rational design of ZnO-NW morphology are not fully explored.

Here we present a systematical investigation on the configurations of paper-based ZnO-NW-enhanced EIS biosensors, in pursuit of optimal sensing performance. Our investigation starts with exploring Faradaic and non-Faradaic EIS processes, and the electron mediators for the Faradaic EIS processes were then chosen through comparison. Three ZnO-NW morphologies were generated by tuning the hydrothermal growth parameters, and EIS biosensors with different ZnO-NW morphologies were calibrated for detection of HIV p24 antigen. Further analyses with scanning electron microscopy (SEM) and electrochemical measurements indicate the relationship between the sensing performance and the surface area of the ZnO-NW-enhanced WE. With the optimal ZnO-NW morphology, we demonstrate that these EIS nanobiosensors can be applied to the serological testing of the IgG antibody (CR3022) specific to SARS coronavirus 2 (SARS-CoV-2) for the diagnosis of COVID-19. Our results offer insights into the rational design of paper-based ZnO-NW-enhanced EIS biosensors, which can facilitate the diagnosis in response to outbreaks of infectious diseases.

2. Experimental methods

2.1. Fabrication of paper-based biosensors

The fabrication of electrochemical μPADs was described in our previous reports (Li et al., 2015b; Li and Liu, 2016). In brief, chromatography #1 paper was patterned by wax printing and subsequent heating to generate confined hydrophilic areas for electrochemical reactions (i.e., reaction zones). A counter electrode (CE) and a reference electrode (RE) were formed in each reaction zone by screen-printing carbon and silver/silver chloride inks, respectively. This layer of paper was then stacked with a layer of WE to form a complete μPAD for electrochemical measurements.

2.2. ZnO-NW-enhanced WEs

Chromatography #1 paper was cut into the shape of WEs by a laser cutter (Fig. 1). One side of the paper piece was then fully covered by carbon ink, and a ZnO nanoparticle (NP) colloidal solution was dropped onto the circular area of this side. ZnO NWs were subsequently grown through a hydrothermal process (Li et al., 2015a). An aqueous solution for the hydrothermal growth contained zinc nitrate hexahydrate to provide zinc composition in ZnO NWs, and hexamethylenetetramine as a mediator. Ammonium hydroxide was added to the growth solution to favor the growth of ZnO NWs from the ZnO-NP-seeded cellulose fibers of paper. The morphology of ZnO NWs can be controlled by adjusting the chemical composition of the growth solution and the growth time, as discussed in sections to follow. After the ZnO-NW growth, a surface chemistry process was accomplished to functionalize the WEs. In the process, ZnO-NW-enhanced WEs were treated with air plasma, a 2.5% (v/v) glutaraldehyde solution, a 10 mM (3-aminopropyl)trimethoxysilane ethanol solution, a solution of probe molecules (e.g., 10 μg ml^{-1} HIV p24 antibody), and eventually a commercial blocking reagent (cat. no. 11152500, Roche) (Li and Liu, 2016).

2.3. Electrochemical measurements

A potentiostat (Autolab PGSTAT302N, Metrohm) was used in this study to implement electrochemical measurements. In EIS measurements, samples with varied p24 antigen concentrations were dropped to the surface-functionalized WEs. After 15-min incubation, the WEs were cleaned with 5 μl of 1× phosphate-buffered saline (PBS) containing 0.05% (v/v) Tween 20 (cat. no. P9416, Sigma-Aldrich). Then each WE was attached to a layer of reaction zone containing a set of CE and RE. After 4 μl of electron mediator solution was dropped into the reaction zone, an EIS measurement was performed (Li and Liu, 2016). In cyclic voltammetric (CV) measurements, there were no sample addition and washing steps.

2.4. Serological antibody testing for COVID-19 with human serum samples

To prepare the EIS nanobiosensors for serological antibody testing for COVID-19, ZnO-NW-enhanced WEs were surface-functionalized with probe molecules specific to the COVID-19 antibody. Specifically, 3 μl of SARS-CoV-2 S-protein receptor-binding domain (RBD) was immobilized on the WEs through the surface functionalization process described previously and incubated in a 4 °C fridge for 4 h (Li and Liu, 2016). The WEs were later washed with 8 μl of PBS and blocked with 3 μl of a blocking reagent (cat. no. 11112589001, Roche). The washing and blocking steps were repeated twice with an interval of 30 min. The surface-functionalized WEs were then washed by 8 μl of PBS with 0.05% (v/v) Tween 20. To prepare human serum samples for testing, recombinant IgG antibody (CR3022) to SARS-CoV-2 spike glycoprotein S1 was spiked at different concentrations in human serum (cat. no. P2918, Sigma-Aldrich) to mimic the real patient samples. Both the RBD protein and the CR3022 antibody were synthesized by James Rini's laboratory at the University of Toronto.

During a test for COVID-19, 3 μl of spiked human serum was applied onto a WE. The sample was incubated at room temperature for 15 min and washed with 5 μl of PBS containing 0.05% (v/v) Tween 20. The WE was assembled into a complete μPAD with a reaction zone, a CE, and an RE. In an EIS measurement, 4 μl of electron mediator solution was added to the reaction zone. The electron mediators were prepared with 5 mM $K_3[Fe(CN)_6]$ (cat. no. 244023, Sigma-Aldrich) and 5 mM $K_4[Fe(CN)_6]$ (cat. no. P3289, Sigma-Aldrich) in 100 mM KCl solution (cat. no. POC308.1, Bioshop).

3. Results and discussion

3.1. Paper-based EIS biosensors for managing the pandemics of infectious diseases

In the outbreaks of infectious diseases like COVID-19, identifying infected persons, providing medical attention, and practicing appropriate quarantine are crucial to curbing the spread of diseases. Although standard laboratory tests are available, such as polymerase chain reaction (PCR) based testing of SARS-CoV-2 and ELISAs for serological testing of antibodies to SARS-CoV-2, they are usually equipment-dependent, technician-requiring, time-consuming, and expensive. These characteristics of the laboratory tests make them less accessible for POC diagnosis in non-laboratory settings, such as doctors' offices, long-term care homes, cruise ships, and ports of entry. Therefore, it is critical to develop diagnostic tools that are not only accurate but also easy-to-operate and low-cost to identify virus carriers, especially asymptomatic carriers.

Aiming at POC diagnosis, we propose to enhance the EIS sensing performance on μPADs for the detection of proteins related to infectious diseases including COVID-19. Conventionally, ELISAs are widely used in clinical tests for detecting these proteins, and researchers have integrated ELISA-like assays into μPADs (Cheng et al., 2010; Fu et al., 2019; Martinez, 2011). However, these ELISA-based biosensors commonly require labeling and extra steps to generate and amplify the sensing signals, making the biosensors less user-friendly. The extra steps also make the biosensors subject to errors and instability. In contrast, EIS biosensing does not require labels and can be highly sensitive, because EIS differentiates electrical components on the surface of WEs. Therefore, we consider EIS biosensing to be a potentially preferable approach to protein detection for infectious diseases including COVID-19.

EIS biosensors belong to the category of so-called affinity-based biosensors, where target molecules bind to probe molecules on a transducer (Daniels and Pourmand, 2007; Luo and Davis, 2013). The EIS-based biosensing mechanisms remove the need for labeling the target molecules and thus simplifies biosensing operations. Compared to other electrical biosensors that measure only the current (amperometry) or voltage (voltammetry) changes in the binding events, EIS biosensors measure the impedance in an alternating current (AC) steady state with a constant direct current (DC) bias, presenting a spectrum that distinguishes the components on the surface of transducers (i.e., WEs). The binding events are typically associated with an increase of specific resistance components, which contributes to the high sensitivity of EIS biosensors.

In addition to the simplicity and high sensitivity of the proposed sensing method for virus-caused infectious diseases, the low cost of the proposed biosensors would make the rapid diagnosis more accessible to economically disadvantaged regions. First, μPADs are made of paper, which is a relatively cheap substrate material, and their fabrication does not require microfabrication techniques as conventional microfluidic chips do. Second, we proposed a hydrothermal growth method that is facile and requires no expensive facilities so that the addition of ZnO NWs to the μPADs retain their merit of low-cost fabrication. Third, the EIS method we proposed removes the need for extra labeling or signal-amplifying chemicals; thus, the reagents in this sensing method would cost less than conventional ELISAs or other highly sensitive methods based on amplifying reagents. Overall, we estimate the cost of each test to be CAD $0.1, based on the amounts of reagents involved in each test and the price of paper substrates.

3.2. Preparation of ZnO-NW-enhanced WEs

The WEs used in this study were made with laser-cut paper pieces and carbon ink. Before any treatment, the surface of a carbon-ink-coated paper piece had a non-smooth morphology (Fig. S1). As shown in the inset of Fig. 1, the hydrothermal growth process generated ZnO NWs fully covering the surface of carbon ink. Three growth conditions were utilized to generate varied morphologies of ZnO NWs (Table S1), which were named as a combination of their relative width (thick, medium, and thin) and length (long, medium, and short). The concentrations of zinc nitrate hexahydrate and hexamethylenetetramine were changed proportionately, and lower concentrations led to thinner ZnO NWs. Ammonium hydroxide was used as a buffer to suppress homogeneous nucleation of ZnO in the growth solution and favor heterogeneous nucleation on ZnO-NP-seeded paper substrates (Li et al., 2015a; Xu et al., 2009). We adjusted the growth time up to 8 h, as the growth rate significantly decreases after this time (Li et al., 2015b).

The efficacy of affinity-based biosensor relies on the stable immobilization of probe molecules and the blocking reagent to minimize non-specific binding. In this study, an organosilane-based surface chemistry process was used to introduce probe molecules to the surface of ZnO NWs. A blocking reagent was applied to eliminate non-specific binding when capturing target molecules. This surface functionalization process has proved effective in our previous study (Li and Liu, 2016).

3.3. Examining different EIS settings

EIS biosensing has been applied to microscale systems (Jin et al., 2017; Nguyen et al., 2013; Selvam et al., 2017), and researchers

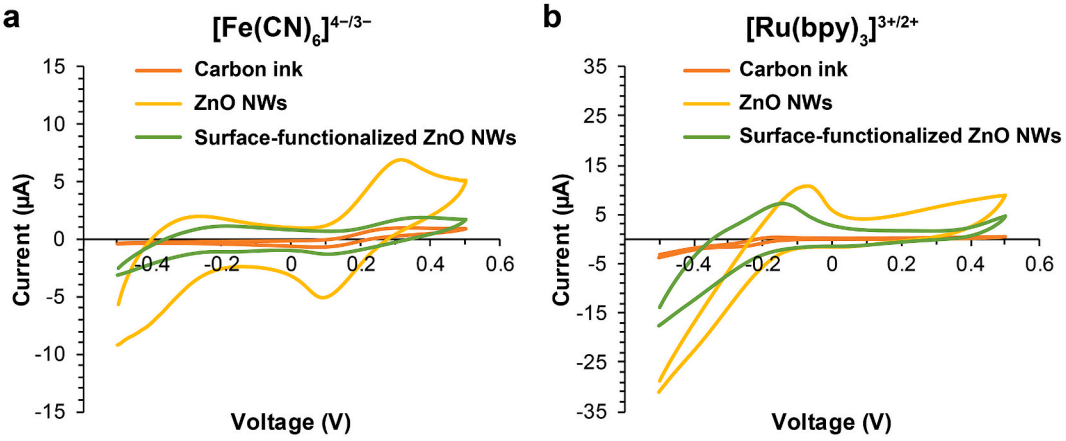

Fig. 2. CV results of WEs with different electron mediators. (a, b) Three WE conditions were tested for $[Fe(CN)_6]^{4-/3-}$ (a) and $[Ru(bpy)_3]^{3+/2+}$ (b): pristine carbon-ink WEs, ZnO-NW-enhanced WEs, and surface-functionalized ZnO-NW-enhanced WEs.

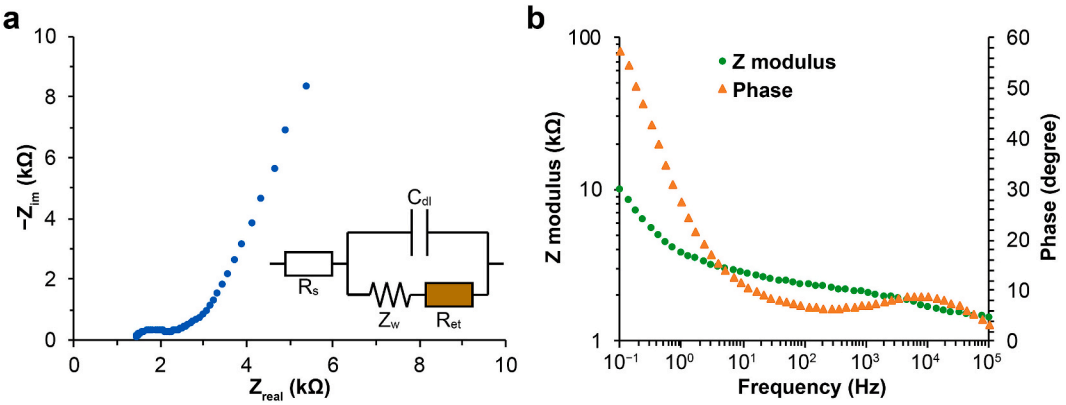

Fig. 3. EIS results and circuit analysis of ZnO-NW-enhanced WEs. (a) A representative Nyquist plot from EIS measurements and the corresponding circuit model. R_s, C_{dl}, R_{et}, and Z_w denote the resistance of solution, the capacitance of the electrical double layer on WE surface, the resistance of electron transfer, and the Warburg impedance, respectively. (b) Representative modulus and phase results from EIS measurements plotted against AC frequencies.

reported improved sensing performance using WEs enhanced by nanomaterials, such as gold nanoparticles and carbon nanotubes (Fayazfar et al., 2014; Yang et al., 2013). We reported the first design of μPADs with ZnO-NW-enhanced WEs for EIS-based detection of protein disease markers (Li and Liu, 2016). Compared to bulk solutions and pump-driven microfluidic devices, the liquid environment held by cellulose fibers of paper substrates forms a different type of electrochemical cell, in terms of the diffusion rates of electrolytes and the evaporation rates of liquids. Therefore, the settings of EIS for μPADs require tuning to achieve stable performance.

To improve EIS settings for μPADs, we first examined non-Faradaic and Faradaic processes. As shown in Fig. S2, non-Faradaic processes performed with PBS did not generate stable Nyquist plots from EIS measurements; therefore, we moved our focus to Faradaic processes, for which both negatively charged $[Fe(CN)_6]^{4-/3-}$ and positively charged $[Ru(bpy)_3]^{3+/2+}$ were examined as electron mediator candidates. We tested three WE conditions for each pair of electron mediators through CV measurements: pristine carbon-ink WEs, ZnO-NW-enhanced WEs, and surface-functionalized ZnO-NW-enhanced WEs. CV measurements are expected to display clear redox peaks of a pair of electron mediators, and the middle point of the redox peaks can be used as the constant DC bias in EIS measurements. The obtained CV results are shown in Fig. 2. With the pristine carbon WEs, both pairs of electron mediators showed clear redox peaks. ZnO NWs on WEs substantially elevated the current readouts probably because of their large surface areas and high electron transfer rate, whereas the introduction of insulating molecules through surface functionalization dampened the current. We noted that the anodic peaks of $[Ru(bpy)_3]^{3+/2+}$ were missing from both ZnO-NW-enhanced WEs and surface-functionalized ZnO-NW-enhanced WEs. This may be a result of the interaction between $[Ru(bpy)_3]^{3+/2+}$ ions and positively charged ZnO-NW surface in physiological solution (Pradhan et al., 2010). In the light of these experimental results, we chose the Faradaic processes with $[Fe(CN)_6]^{4-/3-}$ as the pair of electron mediators.

3.4. Examining the effects of ZnO NWs on EIS measurements

One-dimensional NWs brings apparent morphological changes to the surface of carbon-ink WEs. We examined how this morphological transition affects EIS results. For comparison, we first tested carbon-ink WEs and ZnO-NP-coated WEs, which were both surface-functionalized. As shown in Fig. S3, the Nyquist plots of these WEs were fluctuating. Thick-long ZnO NWs with surface functionalization, on the other hand, exhibited reliable Nyquist plots (Fig. 3a). The instability of carbon-ink and ZnO-NW-coated WEs mainly occurred at low AC frequencies, and this frequency range illustrates the electrical resistance part of the impedance. Therefore, we postulate that surface functionalization degenerates the conductivity of WEs. In line with our postulation, ZnO NWs lowered the resistance of WEs even after surface functionalization (Fig. 2), which led to the reliable EIS results of ZnO-NW-enhanced WEs.

The circuit model for interpreting the EIS results of ZnO-NW-enhanced WEs is displayed in Fig. 3a. The impedance of the circuit

Table 1
Morphological dimensions of ZnO NWs (mean ± standard deviation).

ZnO-NW morphology	Width (n = 50)	Length (n = 50)	Density (n = 20)	Surface area of individual NWs	Surface area ratio
#1 (Thick-long)	295.95 ± 92.53 nm	2431.67 ± 884.62 nm	6.9 ± 1.02 μm^{-2}	2.33 μm^2	16.81
#2 (Thin-medium)	137.57 ± 27.84 nm	1485.479 ± 331.59 nm	13.65 ± 1.39 μm^{-2}	0.66 μm^2	8.97
#3 (Medium-short)	155.05 ± 22.08 nm	1221.31 ± 262.56 nm	13.1 ± 1.48 μm^{-2}	0.614 μm^2	8.04

can be expressed as

$$Z = Z_{R_s} + \frac{1}{\frac{1}{Z_{C_{dl}}} + \frac{1}{Z_{R_{et}} + Z_w}},$$

where

$$Z_{R_s} = R_s,$$

$$Z_{C_{dl}} = \frac{-j}{\omega C_{dl}},$$

$$Z_{R_{et}} = R_{et},$$

$$Z_w = \frac{\sigma}{\sqrt{\omega}}(1 - j),$$

ω is the angular frequency.

σ is the Warburg constant.

The obtained Nyquist plots feature a dome at high frequencies, and the diameter of the dome corresponds to the resistance of electron transfer (R_{et}). The impedance modulus and phase plots are shown in Fig. 3b, where modulus decreased with AC frequencies and phase became greater around 10 kHz.

3.5. Examining the effect of ZnO-NW morphology on EIS biosensing

By taking advantage of the hydrothermal growth process, we explored the performance of paper-based EIS biosensors with varied ZnO-NW morphologies. As described previously, three ZnO-NW morphologies were generated in this study (Table 1, Fig. 4a). Fig. 4b shows Nyquist plots obtained with thick-long ZnO-NW-enhanced WEs, after PBS samples with varied p24 antigen concentrations were tested. The diameters of the dome regions (corresponding to the resistance of electron transfer) increased at high p24 antigen concentrations, and the resistance of electron transfer was used as the biosensing readouts accordingly. Calibration experiments with three different ZnO-NW morphologies were performed, and the calibration curves are shown in Fig. 4c, d, and e. Over the same p24 antigen concentration range, thick-long ZnO NWs generated the biggest resistance change (about 3 kΩ), and there was no apparent saturation up to the concentration of 1 μg ml^{-1}. In contrast, thin-medium and medium-short ZnO NWs led to relatively small resistance changes over the concentration range (about 2 kΩ for thin-medium ZnO NWs and about 1.3 kΩ for medium-short ZnO NWs). In particular, their responses to high p24 antigen concentrations diminished, which is a sign of getting saturated. With the calibration curves in Fig. 4, we calculated the limits of detection (LODs) of these EIS nanobiosensors. Specifically, we referred to triple the standard deviation of the blank samples and determined the corresponding sample concentration in a calibration curve as the LOD. As labelled in Fig. 4c, d, and e, the LODs achieved with the thick-long, thin-medium, and medium-short ZnO NWs were 0.4 pg ml^{-1}, 2.3 pg ml^{-1}, and 1.2 ng ml^{-1}, respectively.

3.6. Surface area analyses for improving EIS biosensing

The calibration results with three ZnO-NW morphologies suggest ZnO-NW morphology affects the sensing performance. In order to understand this relation, we analyzed the surface areas of the three ZnO-NW morphologies through microscopic imaging and electrochemical measurements.

The surface areas of ZnO NWs were first calculated based on SEM imaging (Fig. 4a). The width and length differences across the ZnO-NW morphologies are discernible in the images. To estimate the total surface area of ZnO NWs over a nominal area, we considered the ZnO NWs as cylinders. The thickness of a ZnO NW in the middle of its length was assumed to be the diameter of the cylinder. The surface areas of individual NWs and surface area ratios (the total surface area of ZnO NWs on a WE divided by the nominal area of the WE) are organized in Table 1. Thick-long ZnO NWs have a significantly higher surface area ratio (16.81) compared to the other two morphologies, while the medium-short ZnO NWs have the smallest surface area ratio (8.04).

We then performed CV measurements to probe the electrochemical surface areas of ZnO-NW-enhanced WEs (Fig. S4). The cathodic current peaks obtained from CV measurements were fitted into linear regressions, as shown in Fig. 4f. According to the Randles-Sevcik equation, the coefficients of the linear regressions are proportional to electrochemical surface areas, assuming the diffusion coefficients of electron mediators are the same for the three ZnO-NW morphologies. The electrochemical surface areas (reflected as the slopes of fitting lines in Fig. 4f) of the ZnO-NW morphologies displayed a trend similar to their morphological surface areas (Table 1): while all the ZnO NWs substantially increased the surface areas of pristine carbon-ink WEs (22.755), thick-long ZnO NWs (210.73) increased the surface areas more than the other two ZnO-NW morphologies (82.059 for thin-medium ZnO NWs and 62.493 for medium-short ZnO NWs).

The results from HIV p24 antigen calibrations and the two surface area analyses show that greater ZnO-NW surface areas led to higher saturation levels and sensitivities in EIS biosensing. For example, thick-long ZnO NWs exhibited the highest surface area ratio among the three ZnO-NW morphologies, and they generated a greater response to high HIV p24 antigen concentrations and a better LOD compared to the other two ZnO-NW morphologies. These results are consistent with the previous studies where nanomaterials were used to elevate surface areas and consequently sensing performance (Fayazfar et al., 2014; Yang et al., 2013). In the future, one can estimate the difference in the sensing performance of ZnO NW morphologies through the microscopic imaging and electrochemical measurements we presented here. Our results also indicate the possibility of further boosting the performance of ZnO-NW EIS biosensors by increasing the surface areas of ZnO NWs. For example, alternative compositions of hydrothermal growth solutions may be explored to generate ZnO-NW morphologies that exhibit greater surface areas. Replenishing the hydrothermal growth solution before the depletion of reagents may extend the growth of ZnO NWs, but it is worth noting that the tips of long ZnO NWs may contact each other, which limits their further growth. Therefore, fine-tuning the seeding density of ZnO NPs and the growth condition of ZnO NWs will be necessary for maximizing the total surface areas of ZnO NWs.

In Table S2, we compare the performance of ZnO-NW-enhanced EIS biosensors in this work with commercial ELISA kits and previously reported biosensors. Different from commercial ELISA kits (Tang and Hewlett, 2010), the presented EIS nanobiosensors provide better LODs, cost less, and can be finished in a much shorter period of time. In comparison to other biosensors that utilize paper substrates (Wang et al., 2020) or ZnO-nanostructures-enhanced EIS measurements (Perumal et al., 2015), the approach presented here combines the benefits of these factors to achieve both high sensitivity and low cost.

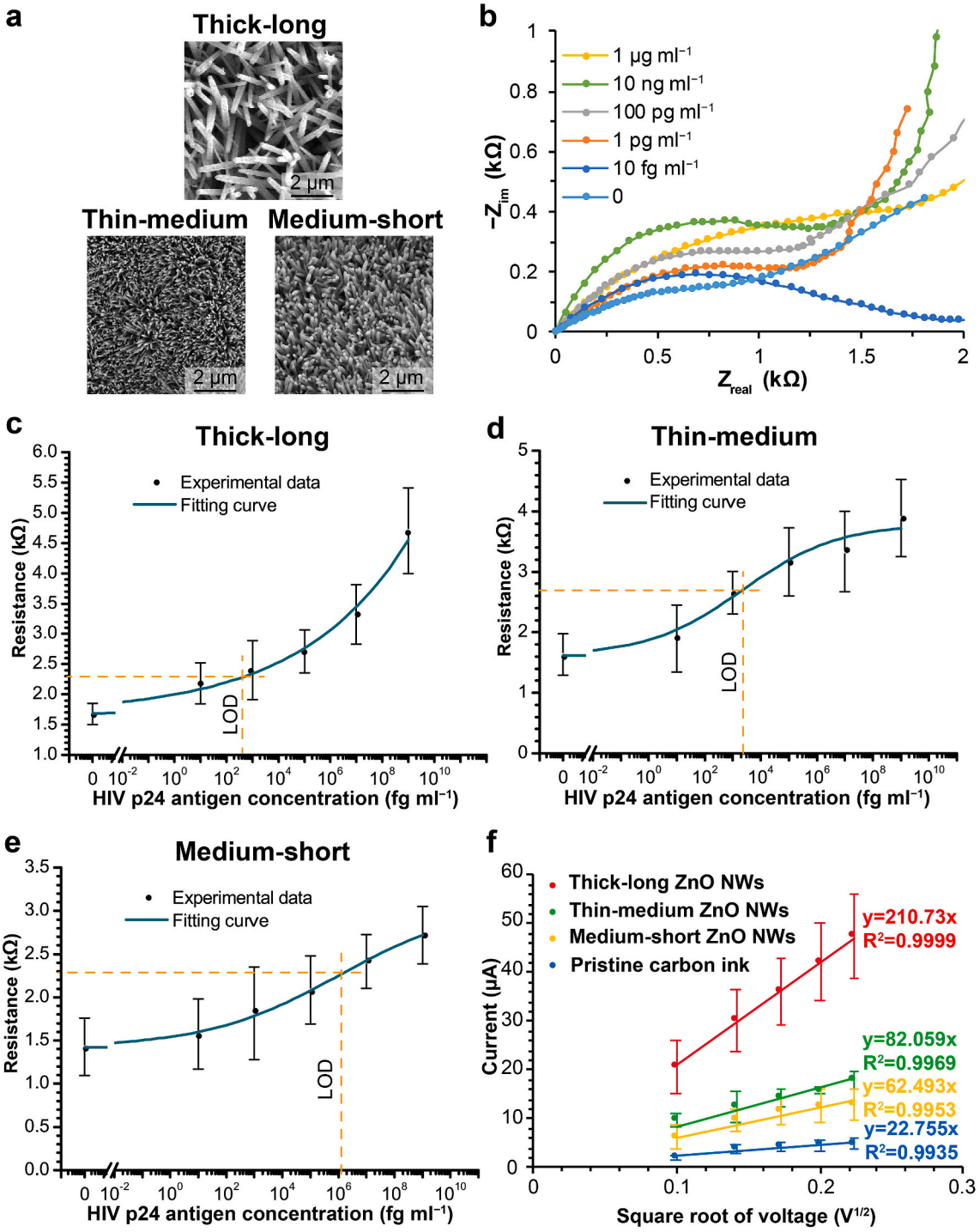

Fig. 4. Calibration results and surface area analyses with varied ZnO-NW morphologies. (a) SEM images of thick-long, thin-medium, and medium-short ZnO NWs grown on WEs. (b) Nyquist plots in response to HIV p24 antigen concentrations. The plots are repositioned to (0, 0) for better comparison. (c–e) Calibration results of EIS biosensors with three ZnO-NW morphologies. The calibration results were fitted into curves based on the Hill equation. Orange dash lines indicate the LODs of these calibrations, based on triple the standard deviations of blank samples in the corresponding calibrations. (f) CV results from varied ZnO-NW morphologies. Linear fitting equations are shown for pristine carbon ink (blue), medium-short ZnO NWs (yellow), thin-medium ZnO NWs (green), and thick-long ZnO NWs (red), respectively. All error bars represent standard deviations (n = 5). (For interpretation of the references to colour in this figure legend, the reader is referred to the Web version of this article.)

3.7. Serological antibody testing for COVID-19

Different from nucleic-acid-based tests utilizing PCR to detect the viral genetic material in throat or nasal swabs (Udugama et al., 2020), serological antibody tests reveal the existence of immunological antibodies in blood caused by the viral infection (Lipsitch et al., 2020). Although PCR-based viral detection is sensitive and can effectively confirm the early SARS-CoV-2 infection (Qin et al., 2020), the virus-specific antibody detection for COVID-19 is also important for the following reasons. (1) Antibody tests do not require PCR-like sample preparation and thus can be more efficient. (2) They can complement nucleic acid tests for the diagnosis of suspected cases with negative PCR

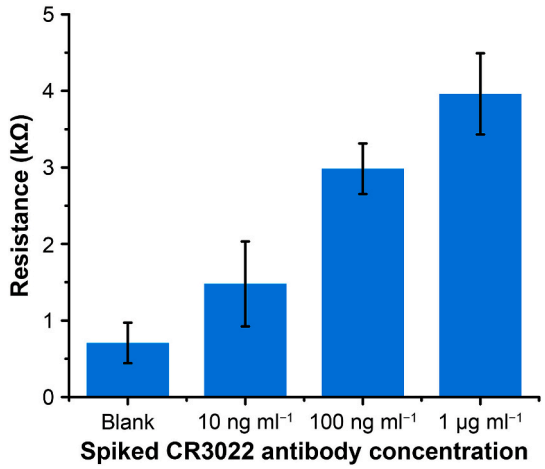

Fig. 5. Experimental results of detecting CR3022 antibody (specific to SARS-CoV-2 spike glycoprotein S1) in human serum. Error bars represent standard deviations (n = 5).

results. (3) They can survey for asymptomatic infection to control the virus spread (Tang et al., 2020). In particular, the paper-based EIS biosensing approach presented here features low cost, high sensitivity, and convenience, which could make the COVID-19 antibody tests more accessible.

Recent research has shown that IgM and IgG antiviral antibodies can be detected in the serum samples of patients infected with SARS-CoV-2 (Ma et al., 2020; Teng et al., 2020). In this work, we employed our EIS nanobiosensors for the detection of CR3022 antibody (specific to SARS-CoV-2 RBD) in human serum. The assay protocol was the same as the HIV p24 antigen tests, which can be finished in 30 min. As shown in Fig. 5, the test results confirm that the paper-based EIS nanobiosensors can differentiate the human serum samples spiked at different CR3022 antibody concentrations (blank, 10 ng ml^{-1}, 100 ng ml^{-1}, 1 μg ml^{-1}). These results demonstrated the feasibility of our EIS nanobiosensors for COVID-19 diagnosis.

4. Conclusion

In this work, we reported an experimental method to improve the performance of paper-based ZnO-NW-enhanced EIS biosensors. The method of directly synthesizing ZnO NWs on μPADs not only retains the facile fabrication and low cost of μPADs but also allows the convenient fine-tuning of ZnO-NW morphology as an approach to better sensing performance. We showed that the ZnO-NW-enhanced EIS biosensors achieved high sensitivity for the detection of HIV p24 antigen (LOD down to 0.4 pg ml^{-1}). Our analyses based on SEM and electrochemical measurements revealed that the enhancement of sensing performance could be attributed to the morphological and electrochemical surface areas achieved by specific ZnO-NW morphologies. We also demonstrated the capability of the EIS nanobiosensors for detecting CR3022 antibody specific to the spike glycoprotein S1 of SARS-CoV-2 in human serum as a marker for COVID-19. This work advances the understanding of nanomaterial-enhanced EIS biosensing and sheds light on possible avenues to superior EIS biosensing performance by tuning nanomaterial morphology. Such high-performance paper-based nanobiosensors can support accurate and rapid diagnosis for managing the crises of infectious diseases.

CRediT authorship contribution statement

Xiao Li: Investigation, Formal analysis, Writing - original draft, Conceptualization, Methodology. **Zhen Qin:** Investigation, Formal analysis, Writing - original draft. **Hao Fu:** Investigation, Formal analysis. **Ted Li:** Investigation, Formal analysis. **Ran Peng:** Investigation. **Zhijie Li:** Investigation. **James M. Rini**: Investigation, Project administration Supervision, Funding acquisition. **Xinyu Liu**: Investigation, Writing, Conceptualization, Supervision, Project administration, Funding acquisition.

Declaration of competing interest

The authors declare that they have no known competing financial interests or personal relationships that could have appeared to influence the work reported in this paper.

Acknowledgements

This research was supported by the Natural Sciences and Engineering Research Council of Canada (NSERC) (Grant No. RGPIN-2012-418553, RGPIN-2017-06374, RGPAS-2017-507980, and DGDND-2017-00001). X. Li thanks the NSERC-CREATE Training Program in Integrated Sensor Systems and the Banting Postdoctoral Fellowships Program.

Appendix A. Supplementary data

Supplementary data to this article can be found online at https://doi.org/10.1016/j.bios.2020.112672.

References

Bhutta, Z.A., Sommerfeld, J., Lassi, Z.S., Salam, R.A., Das, J.K., 2014. Infect. Dis. Poverty. 3, 21.
Cheng, C.-M., Martinez, A.W., Gong, J., Mace, C.R., Phillips, S.T., Carrilho, E., Mirica, K. A., Whitesides, G.M., 2010. Angew Chem. Int. Ed. Engl. 49, 4771–4774.
Chen, L., Ying, B., Song, P., Liu, X., 2019. Adv. Mater. Interfaces. https://doi.org/10.1002/admi.201901346.
Daniels, J.S., Pourmand, N., 2007. Electroanalysis 19, 1239–1257.
Fayazfar, H., Afshar, A., Dolati, M., Dolati, A., 2014. Anal. Chim. Acta 836, 34–44.
Fu, H., Song, P., Wu, Q., Zhao, C., Pan, P., Li, X., Li-Jessen, N.Y.K., Liu, X., 2019. Microsyst. Nanoenergy 5, 50.
Gong, M.M., Sinton, D., 2017. Chem. Rev. 117, 8447–8480.
Jin, S., Ye, Z., Wang, Y., Ying, Y., 2017. Sci. Rep. 7, 43175.
Lipsitch, M., Kahn, R., Mina, M.J., 2020. Nat. Med. 26, 818–819.
Li, X., Liu, X., 2016. Adv. Healthc. Mater. 5, 1378.
Li, X., Wang, Y.-H., Lu, A., Liu, X., 2015a. IEEE Sensor. J. 15, 6100–6107.
Li, X., Zhao, C., Liu, X., 2015b. Microsyst. Nanoenergy 1, 15014.
Luo, X., Davis, J.J., 2013. Social. Rev. 42, 5944–5962.
Ma, H., Zeng, W., He, H., Zhao, D., Jiang, D., Zhou, P., Cheng, L., Li, Y., Ma, X., Jin, T., 2020. Cell. Mol. Immunol. 17, 773–775.
Martinez, A.W., 2011. Bioanalysis 3, 2589–2592.
Martinez, A.W., Phillips, S.T., Whitesides, G.M., Carrilho, E., 2010. Anal. Chem. 82, 3–10.
McBain, R.K., Jerome, G., Warsh, J., Browning, M., Mistry, B., Faure, P.A.I., Pierre, C., Fang, A.P., Mugunga, J.C., Rhatigan, J., Leandre, F., Kaplan, R., 2016. BMJ Global Health 1, e000134.
Nguyen, T.A., Yin, T.-I., Reyes, D., Urban, G.A., 2013. Anal. Chem. 85, 11068–11076.
Perkins, M., 2011. Pathology 43, S3–S4.
Perumal, V., Hashim, U., Gopinath, S.C.B., Haarindraprasad, R., Foo, K.L., Balakrishnan, S.R., Poopalan, P., 2015. Sci. Rep. 5, 12231.
Pradhan, D., Niroui, F., Leung, K.T., 2010. ACS Appl. Mater. Interfaces 2, 2409–2412.
Qin, Z., Peng, R., Baravik, I.K., Liu, X., 2020. Matter 3, 628–651.
Rengaraj, S., Cruz-Izquierdo, Á., Scott, J.L., Di Lorenzo, M., 2018. Sensor. Actuator. B Chem. 265, 50–58.
Rolland, J.P., Mourey, D.A., 2013. MRS Bull. 38, 299–305.
Ruecha, N., Shin, K., Chailapakul, O., Rodthongkum, N., 2019. Sensor. Actuator. B Chem. 279, 298–304.
Selvam, A.P., Wangzhou, A., Jacobs, M., Wu, T., Mohan, C., Prasad, S., 2017. Future Sci. OA 3, FSO224.
Sher, M., Zhuang, R., Demirci, U., Asghar, W., 2017. Expert Rev. Mol. Diagn. 17, 351–366.
Tang, S., Hewlett, I., 2010. J. Infect. Dis. 201 (Suppl. 1), S59–S64.
Tang, Y.-W., Schmitz, J.E., Persing, D.H., Stratton, C.W., 2020. J. Clin. Microbiol. 58 https://doi.org/10.1128/JCM.00512-20.
Teng, J., Dai, J., Su, Y., Zhou, Z., Chi, H., Wan, L., Meng, J., Wang, Z., Wang, F., Ma, Y., Hu, Q., Cheng, X., Liu, H., Ye, J., Shi, H., Sun, Y., Yang, C., Wang, X., 2020. Lancet Rheumatol 2, E384–E385.
Udugama, B., Kadhiresan, P., Kozlowski, H.N., Malekjahani, A., Osborne, M., Li, V.Y.C., Chen, H., Mubareka, S., Gubbay, J.B., Chan, W.C.W., 2020. ACS Nano 14, 3822–3835.
Wang, C., Horby, P.W., Hayden, F.G., Gao, G.F., 2020. Lancet 395, 470–473.

Wang, Y., Sun, S., Luo, J., Xiong, Y., Ming, T., Liu, J., Ma, Y., Yan, S., Yang, Y., Yang, Z., Reboud, J., Yin, H., Cooper, J.M., Cai, X., 2020. Microsyst. Nanoenergy 6, 32.
Xu, C., Shin, P., Cao, L., Gao, D., 2009. J. Phys. Chem. C 114, 125–129.
Yamada, K., Shibata, H., Suzuki, K., Citterio, D., 2017. Lab Chip 17, 1206–1249.
Yang, H., Li, Z., Wei, X., Huang, R., Qi, H., Gao, Q., Li, C., Zhang, C., 2013. Talanta 111, 62–68.
Yang, Y., Noviana, E., Nguyen, M.P., Geiss, B.J., Dandy, D.S., Henry, C.S., 2017. Anal. Chem. 89, 71–91.
Ying, B., Park, S., Chen, L., Dong, X., Young, E.W.K., Liu, X., 2020. Lab Chip 20, 3322–3333.
Zhao, C., Liu, X., 2016. Biomicrofluidics 10, 024119.
Zhu, N., Zhang, D., Wang, W., Li, X., Yang, B., Song, J., Zhao, X., Huang, B., Shi, W., Lu, R., Niu, P., Zhan, F., Ma, X., Wang, D., Xu, W., Wu, G., Gao, G.F., Tan, W., 2019. N. Engl. J. Med. 382, 727–733.